ChemPubSoc Europe

DOI: 10.1002/chem.201702938

CHEMISTRY A European Journal Communication

Rhodium Complexes | *Hot Paper*

Electrocatalytic Azide Oxidation Mediated by a Rh(PNP) Pincer Complex

Christophe Rebreyend,[a] Yann Gloaguen,[a] Martin Lutz,[b] Jarl Ivar van der Vlugt,[a] Inke Siewert,[c] Sven Schneider,*[c] and Bas de Bruin*[a]

Abstract: One-electron oxidation of the rhodium(I) azido complex [Rh(N_3)(PNP)] (**5**), bearing the neutral, pyridine-based PNP ligand 2,6-bis(di-*tert*-butylphosphinomethyl)-pyridine, leads to instantaneous and selective formation of the mononuclear rhodium(I) dinitrogen complex [Rh(N_2)(PNP)]$^+$ (**9**$^+$). Interestingly, complex **5** also acts as a catalyst for electrochemical N_3^- oxidation ($E_p \approx -0.23$ V vs. $Fc^{+/0}$) in the presence of excess azide. This is of potential relevance for the design of azide-based and direct ammonia fuel cells, expelling only harmless dinitrogen as an exhaust gas.

The Haber–Bosch process involves dinitrogen cleavage on an iron surface, producing two nitrides that subsequently react with dihydrogen to form ammonia.[1] In light of dinitrogen activation, the microscopic reverse reaction, that is, nitride coupling, (2 $M^n \equiv N \rightarrow M^{n-3}-N \equiv N-M^{n-3}$) is of contemporary interest as well. Such N–N coupling reactions are also relevant for development of non-carbon-based fuel cell technologies using nitrogen-based energy-carriers (e.g. ammonia, hydrazine or azide salts). The processes are kinetically accessible and have been described for a number of metals, including examples of group 8 and group 9 transition metal complexes.[2,3]

[a] *C. Rebreyend, Dr. Y. Gloaguen, Dr. Ir. J. I. van der Vlugt, Prof. Dr. B. de Bruin*
Homogeneous and Supramolecular Catalysis
van't Hoff Institute for Molecular Sciences (HIMS)
University of Amsterdam
Amsterdam (The Netherlands)
E-mail: b.debruin@uva.nl

[b] *Dr. M. Lutz*
Crystal and Structural Chemistry
Bijvoet Center for Biomolecular Research
Utrecht University
Padualaan 8, 3584 CH Utrecht (The Netherlands)

[c] *Prof. Dr. I. Siewert, Prof. Dr. S. Schneider*
Universität Göttingen
Institut für Anorganische Chemie
Tammannstr. 4, 37077 Göttingen (Germany)
E-mail: Sven.Schneider@chemie.uni-goettingen.de

The Supporting Information and ORCID identification number(s) for the author(s) of this article can be found under https://doi.org/10.1002/chem.201702938.

Examples involving N–N coupling of nitrido (N^{3-})/nitridyl ($N^{2-\cdot}$) complexes with d^n electron counts of $n \geq 4$ are in all cases strongly exothermic, with the M(N) species involved being usually transient and highly reactive intermediates. Recently, such transient terminal nitrido complexes of rhodium and iridium (**2**) have been spectroscopically characterized.[3b,c] Kinetic studies and DFT calculations revealed that **2** undergoes clean dinuclear nitride-based N–N coupling to form metal(I)–dinitrogen complexes (Scheme 1). This result contrasts with the reactivity of other transient Rh and Co nitrido species, which were reported to yield C–H insertion products,[4] or undergo P–N or C–N bond formation with ligand fragments.[5] Herein, we report the selective conversion of the square planar rhodium(I) azido complex [$Rh^I(N_3)$(PNP)] to the square planar rhodium(I) dinitrogen complex [$Rh^I(N_2)$(PNP)] upon one-electron oxidation (PNP = 2,6-bis(di-*tert*-butylphosphinomethyl)pyridine), and the application of this reaction in electrocatalytic azide oxidation. The latter is of possible relevance for the design and understanding of azide-based and direct ammonia fuel cells, expelling only harmless dinitrogen as exhaust gas. The mechanism of the azide oxidation reaction was explored using electron paramagnetic resonance (EPR), IR spectro-electrochemistry, cyclic voltammetry (CV) simulations and DFT studies.

To explore ligand effects on the reactivity of rhodium azido complexes, we chose to use the neutral PNP pincer ligand (Scheme 2) instead of the mono-anionic PNP pincer ligands previously investigated in the chemistry of [$M^I(N_3)$(PNP)] complexes (M = Rh, Ir; Scheme 1). The corresponding rhodium(I)–chlorido complex [Rh(Cl)(PNP*t*Bu)] was prepared according to a literature procedure.[6] Salt metathesis of this precursor with an excess of NaN_3 afforded the azido complex [Rh(N_3)(PNP*t*Bu)] (**5**) as an analytically pure red powder, in a yield of 68% (Scheme 2). Single crystals suitable for X-ray diffraction studies were obtained by slow evaporation of a benzene solution of **5** at RT. The molecular structure of **5** reveals a square planar coordination geometry around the d^8-rhodium(I) center (Figure 1, left).

Photolysis of rhodium(I)–azido complex **5** (based on the neutral PNP*t*Bu pincer ligand) did not lead to selective reactivity. Instead, a mixture of unidentified products was obtained, even when a large excess of PPh_3 or PCy_3 was added to trap a potential nitrido intermediate. In an attempt to synthesize a cationic analogue of complex **2** ([M(N)(PNP)]), we targeted the synthesis of rhodium(II) azido complex **6**$^+$, which we envisioned would lead to formation of the desired cationic nitridyl

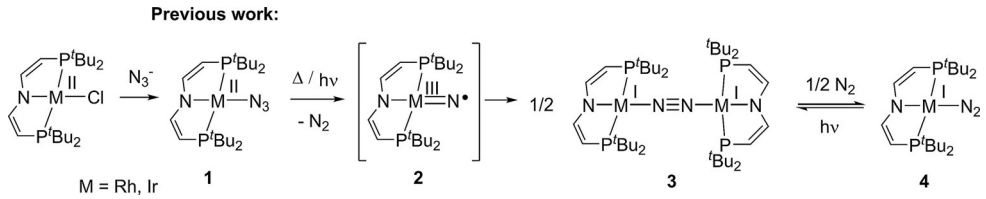

Scheme 1. Formation of square-planar nitrido complexes based on anionic PNP pincer ligands and their N-centered reactivity, leading to N–N coupling.

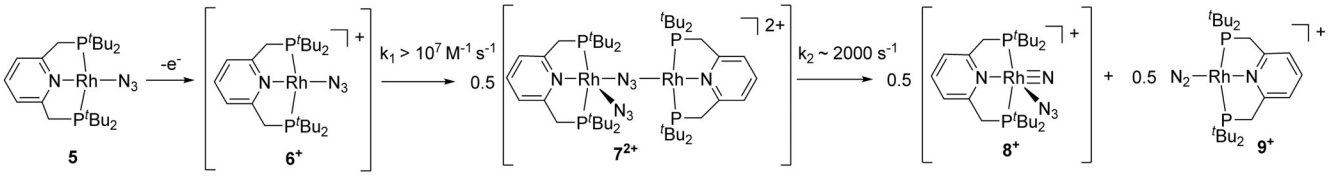

Scheme 2. Proposed reaction pathway after oxidation of **5**, including the formation of transient azido–nitrido intermediate **8**. Rate constants estimated from DFT and CV simulations.

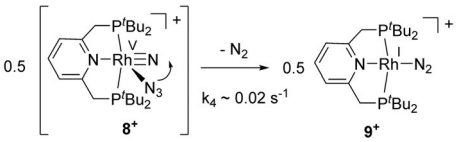

Scheme 3. Further reactivity of nitrido species $\mathbf{8}^+$, forming a second equivalent of $\mathbf{9}^+$.

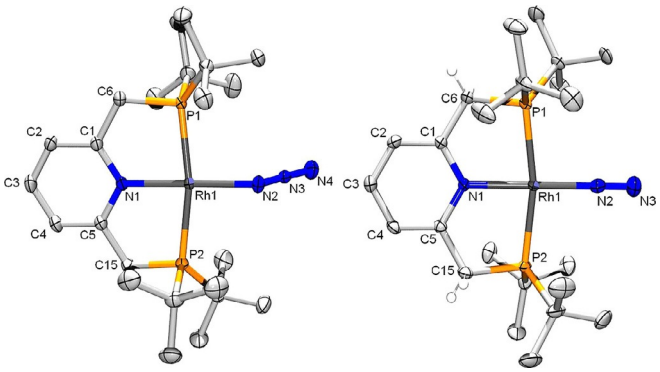

Figure 1. ORTEP plots of the molecular structures of **5** (left) and $\mathbf{9}^+$ (right) (ellipsoids set at 50% probability, hydrogen atoms and PF_6 anion in $\mathbf{9}^+$ are omitted for clarity). Selected bond lengths [Å] and angles [°]: **5**: Rh1–N1 2.0352(14), Rh1–N2 2.0752(15), Rh1–P1 2.2668(4), Rh1–P2 2.2712(4), P1–C6 1.8449(19), C1–C6 1.505(3), N1–C1 1.364(2), N1–C5 1.368(2), C1–C2 1.387(3), C2–C3 1.379(3); C3–C4 1.380(3), C4–C5 1.384(3), N2–N3 1.195(2), N3–N4 1.166(2), N1-Rh1-N2 178.06(6), P1-Rh1-P2 168.036(18). $\mathbf{9}^+$: Rh1–N2 1.916(2), Rh1–N1 2.059(2), Rh1–P1 2.3018(7), Rh1–P2 2.3010(7), N2–N3 1.089(3), N1–C1 1.367(3), N1–C5 1.365(3), C1–C2 1.375(4), C2–C3 1.382(4), C3–C4 1.383(4), C4–C5 1.375(4), N1-Rh1-N2 176.15(10), P1-Rh1-P2 167.27(2), Rh1-N2-N3 176.3(3).

complex $[Rh(N^{\bullet})(PNP^tBu)]^+$ by N_2 loss (either triggered by photolysis or upon heating). However, one-electron oxidation of **5** to $\mathbf{6}^+$ leads to instantaneous formation of the cationic rhodium(I) dinitrogen $[Rh(N_2)(PNP^tBu)]^+$ complex $\mathbf{9}^+$ in the dark. Clearly the targeted cationic rhodium(II)–azido complex $\mathbf{6}^+$ is highly unstable, and spontaneously converts to $\mathbf{9}^+$ in a clean thermal reaction already at room temperature. This is in marked contrast with the thermally more stable neutral species **1** (Rh^{II} and Ir^{II}) bearing an anionic PNP scaffold. Oxidation of rhodium(I) complex **5** with an equimolar amount of $[Fc]PF_6$ at room temperature under exclusion of light immediately afforded the diamagnetic mononuclear rhodium(I)–N_2 adduct $[Rh(N_2)(PNP^tBu)]PF_6$ ($\mathbf{9}^+$) in near-quantitative yield.[7] Complex $\mathbf{9}^+$ was isolated as an analytically pure beige powder (86%) and its structure was confirmed by spectroscopic and crystallographic studies (Figure 1, right). Complex $\mathbf{9}^+$ is a cationic analogue of compound **4**. Similar to the amido pincer complex **4**, the IR spectrum of $\mathbf{9}^+$ exhibits a band of medium intensity corresponding to the N–N stretching vibration (2154 cm^{-1}), and NMR characterization (^{31}P: 70.5 ppm) is also in agreement with C_{2v} symmetry on the NMR time scale in solution.

In marked contrast with the reactions shown in Scheme 1, no trace of a dimeric rhodium complex with a bridging N_2 ligand was detected upon oxidation of complex **5** with ferrocenium salts. Oxidation of **5** under an argon atmosphere with rigorous exclusion of (light and) dinitrogen, also revealed only the presence of the monomeric N_2-complex $\mathbf{9}^+$, according to NMR spectroscopy. EPR experiments in which pre-frozen reagent solutions were thawed, mixed and subsequently immediately re-frozen in liquid nitrogen showed mostly weak EPR signals of a small amount of the dicationic rhodium(II)–N_2 complex $[Rh(N_2)(PNP^tBu)]^{2+}$ ($\mathbf{9}^{2+}$).[8] Another rhodium(II) species that could be detected in smaller amounts under these conditions is the highly unstable monocationic rhodium(II)–azido $[Rh(N_3)(PNP^tBu)]^+$ complex $\mathbf{6}^+$ (see Figures S7–S9, Supporting Information). Variable amounts of this species were detected in several repetition experiments, but always in much lower concentrations than $\mathbf{9}^{2+}$.

The mechanism for the transformation of $\mathbf{6}^+$ into $\mathbf{9}^+$ has proven to be rather complicated according to IR spectro-electrochemistry, CV simulations and DFT studies. Initially we assumed that the conversion would proceed via a similar mechanism as shown in Scheme 1. However, direct N_2 expulsion from $\mathbf{6}^+$ is unlikely according to DFT calculations (see the Support-

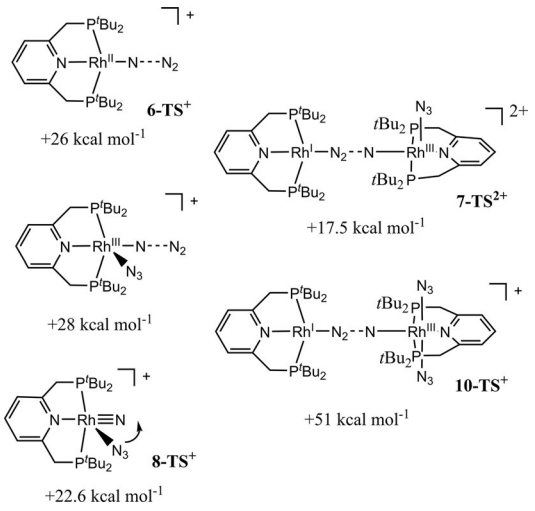

Figure 2. DFT-D3 (BP86, def2-TZVP, COSMO) computed transition states for N_2 elimination and follow-up chemistry.

ing Information), which show that direct N_2-loss from $\mathbf{6}^+$ has a high barrier of $+26$ kcal mol^{-1}. This barrier is too high for an 'instantaneous' reaction at room temperature or below. Several other mono- and dinuclear pathways were explored with DFT (DFT-D3, BP86, def2-TZVP, COSMO), most of which revealing very high barriers for N_2 elimination (Figure 2). Most likely, the actual mechanism involves a rapid (inner-sphere) electron transfer disproportionation step via a dinuclear 1,3-azido-bridged species, generating $[(PNP)Rh^{I}(\mu\text{-}N_3)Rh^{III}(N_3)(PNP)]^{2+}$ or similar species.

Clear evidence that such mixed-valent dinuclear species are formed under the applied reaction conditions was provided by crystallization of the related mixed-valent dinuclear complex $[(PNP)Rh^{I}(\mu\text{-}N_3)Rh^{III}(N_3)_2(PNP)]^+$ ($\mathbf{10}^+$), having captured an additional stabilizing azido ligand. Complex [**10**]PF_6 (co)crystallized in very low yield ($\approx$1%) in the form of a tiny yellow crystal from a 2:1 reaction mixture of **5** and [Fc]PF_6 (Figure 3).

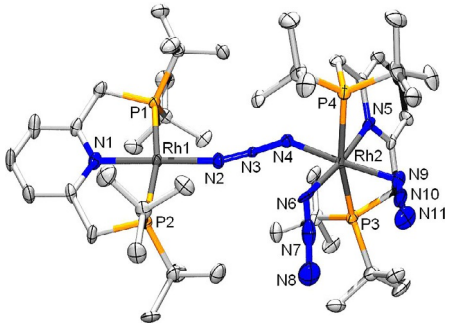

Figure 3. ORTEP plot of the molecular structure of $\mathbf{10}^+$ (ellipsoids set at 50% probability, hydrogen atoms and PF_6 anion of $\mathbf{10}^+$ are omitted for clarity). Rh1–N2 2.012(5), Rh1–N1 2.049(5), Rh1–P2 2.2734(18), Rh1–P1 2.2790(17), Rh2–N5 2.058(5), Rh2–N6 2.068(7), Rh2–N9 2.070(6), Rh2–N4 2.088(5), Rh2–P4 2.3990(18), Rh2–P3 2.4489(19), N2-Rh1-N1 179.7(3), P2-Rh1-P1 168.14(6), N5-Rh2-N6 174.0(2), N9-Rh2-N4 175.7(2), N3-N2-Rh1 165.6(5), N3-N4-Rh2 129.6(4).

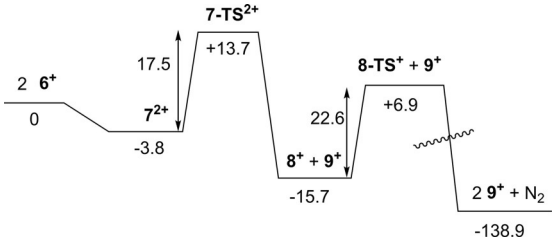

Figure 4. Complete reaction path after oxidation of **5**, as examined with DFT (DFT-D3, def2-TZVP/BP86, COSMO; Free energies (ΔG°_{298} K in kcal mol^{-1})).

Unfortunately, we have not been able to isolate complex [**10**]PF_6 in sufficient amounts for NMR spectroscopic characterization, and large scale synthesis proved unsuccessful, suggesting that $\mathbf{10}^+$ is unstable and decomposes to form $\mathbf{9}^+$ (slower than $\mathbf{6}^+$ and any of the other intermediates shown in Scheme 2).

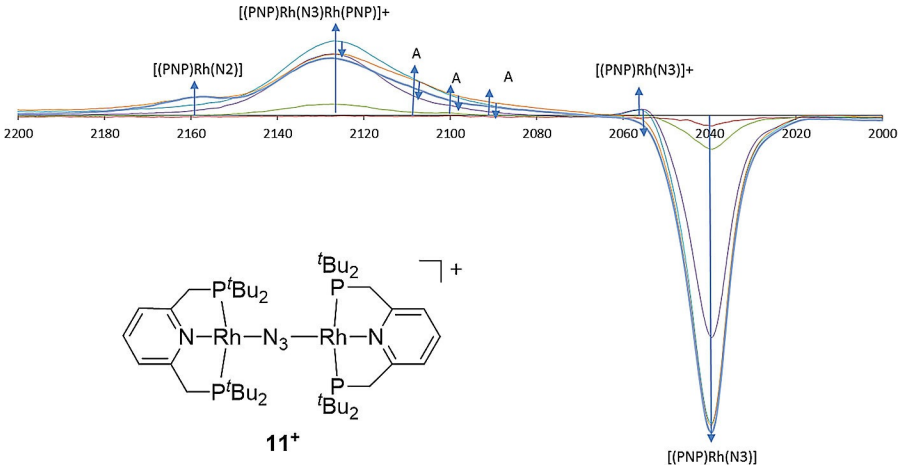

Figure 5. Spectro-electrochemical IR experiments (difference IR spectra) showing the disappearance of species **5** (2031 cm^{-1}) and formation of product $\mathbf{9}^+$ (2157 cm^{-1}), along with a new species at 2130 cm^{-1}, after oxidation ($\mathbf{11}^+$). A shoulder peak at 2056 cm^{-1} indicates the short-lived intermediate species $\mathbf{6}^+$. Additional peaks at 2107, 2099, and 2088 cm^{-1} indicate the presence of one or more additional short-lived intermediates (A), but due to overlap with other more intense bands, assignment of these peaks is complicated.

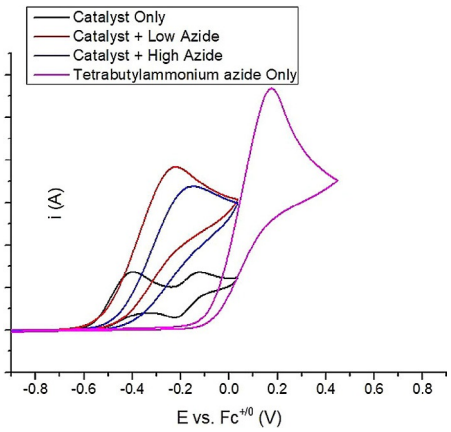

Figure 6. CV experiments carried out with a platinum electrode. a) In black, oxidation of **5** (5.5 mM) in THF, with 0.1 M nBu$_4$PF$_6$; b) In red, oxidation of **5** (5.5 mM) in THF in presence of 19.1 mM nBu$_4$NN$_3$. c) In blue, oxidation of **5** (5.5 mM) in presence of 0.22 M nBu$_4$NN$_3$. d) In pink, oxidation of pure nBu$_4$NN$_3$. Potentials in volt versus Fc$^{+/0}$. Scan rate: 0.1 V s^{-1}.

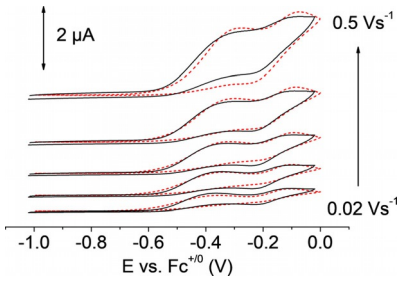

Figure 7. Simulated (black lines) and measured (red dashed lines) CVs of **5** in THF, [nBu$_4$PF$_6$] = 0.1 M, [N$_2$] = 6.4 mM,[12] [**5**] = 4.0 mM.

Based on the observations above, DFT calculations (see also Figure 4 and the supporting information), IR spectro-electrochemical data and CV simulations (see Figures 5–7), we propose the mechanism depicted in Scheme 2 and Scheme 3. Oxidation of **5** generates the rhodium(II)–azido complex **6**$^+$, which has substantial spin density on both Rh and the alpha and gamma nitrogen atoms of the azide moiety (Figure S12, Supporting Information). This facilitates the formation of a 1,3-azido-bridged Rh-μ-N$_3$-Rh dinuclear species by radical–radical coupling of two molecules of **6**$^+$ involving the gamma nitrogen atom of the end-on coordinated azido moiety of one complex and the rhodium atom of another. This leads to the mixed-valent dinuclear complex [(PNP)Rh^{I}(μ-N$_3$)Rh^{III}(N$_3$)(PNP)]$^+$ (**7**$^{2+}$). This is a barrierless process according to DFT (see Supporting Information for details), and can also be described as an inner-sphere electron-transfer disproportionation (Scheme 2). Fragmentation of **7**$^{2+}$ via N–N bond splitting of the bridging azide moiety to form 0.5 equiv. [Rh(N)(N$_3$)(PNP)] (**8**$^+$) and 0.5 equiv. [Rh(N$_2$)(PNP)]$^+$ (**9**$^+$) is exergonic and has a relatively low transition state barrier of +17.5 kcal mol^{-1}, much lower than direct N$_2$ elimination from **6**$^+$ (+26 kcal mol^{-1}). Subsequently, complex **8**$^+$ can produce another 0.5 equiv. of **9**$^+$ by internal coupling of the azido and nitrido moieties, leading to expulsion of dinitrogen with formal reduction of Rh^{V} to Rh^{I} to produce **9**$^+$ (Scheme 3). This process has an accessible transition state barrier (+22.6 kcal mol^{-1}), and is strongly exergonic (Figure 4). Overcoming the **8-TS**$^+$ transition state barrier is facilitated by taking advantage of the energy released in the exothermic first steps of the reaction that produce **8**$^+$ and **9**$^+$ (including oxidation of **5** to **6**$^+$). Precedents for azide–nitride attack exist for osmium.[9]

To gain further insight in in the oxidation of **5** to **9**$^+$, a spectro-electrochemical (SEC) experiment was performed (Figure 5) in which we followed the electrochemical oxidation process with infrared spectroscopy. The SEC-IR spectra clearly show conversion of **5** to **9**$^+$, together with a new species at 2130 cm^{-1} (see Figure 5). This signal is assigned to the dinuclear homovalent azido-bridged rhodium(I) complex [(PNP)Rh^{I}(μ-N$_3$)Rh^{I}(PNP)]$^+$ (**11**$^+$),[10] which is in equilibrium with **5** and **9**$^+$. This was confirmed by a separate infrared measurement in which we mixed **5** and **9**$^+$ in equimolar quantities, showing the same IR peak at 2130 cm^{-1}, together with characteristic IR peaks for **5** and **9**$^+$. Furthermore, the DFT calculated N$_3$ stretching frequency of [(PNP)Rh^{I}(μ-N$_3$)Rh^{I}(PNP)]$^+$ matches the measured value. Although this species has no direct role in the proposed mechanism, it further demonstrates that azido-bridged dinuclear rhodium species are readily formed using these type of compounds.

In agreement with the EPR studies described above, it seems that the [(PNP)Rh^{II}(N$_3$)]$^+$ complex **6**$^+$ can also be detected as an intermediate in small amounts during these SEC-IR measurements, as indicated by a small shoulder at 2056 cm^{-1} appearing and disappearing in the difference IR spectra (Figure 5). The [Rh^{II}(N$_3$)(PNP)] complex **1** (Scheme 1) has a similar azide stretching frequency of 2040 cm^{-1}. Additional weak and transient signals at ≈2107, ≈2099, and ≈2088 cm^{-1} are visible in the SEC-IR experiment, indicating the presence of one or more additional short-lived intermediates. These seem to point to one or more intermediates with bridging azides and/or two azides per Rh atom. Species **8**$^+$ might also have azide stretching vibrations in this region. However, due to spectral overlap with more intense IR bands, unequivocal assignment of these weak signals has so far proven impossible.

Cyclic voltammetry (CV) measurements of **5** reveal an oxidation wave with a peak potential (E_p) of −0.32 V versus Fc$^{+/0}$, followed by a reversible oxidation wave at E = −0.17 V (v = 0.1 V s^{-1}). The latter corresponds to the **9**$^+$/**9**$^{2+}$ redox couple, as confirmed by independent CV measurements of [**9**]PF$_6$ under otherwise identical conditions.

Notably, the peak currents of the **9**$^+$/**9**$^{2+}$ couple, generated in the preceding oxidation process, are practically half of the peak current belonging to the oxidation of **5** (see Figure 6). This is evident over a wide scan rate range, which supports a stepwise formation of **9**$^+$ rather than a nitridyl–nitridyl coupling step as previously reported for similar systems (Scheme 1). In fact, concentration and scan rate dependent CV data could well be simulated applying the two-step mechanism for **9**$^+$ formation as depicted in Scheme 2 and 3 (see Figure 7 for scan rate dependent simulations using 4 mM solutions of **5** (see Supporting Information for further details). The first oxidation wave corresponds to a one-electron oxidation, producing quite rapidly 0.5 equivalent of complex **9**$^+$ and in-

termediate $\mathbf{8}^+$, and more slowly (on the CV time scale) the second half equivalent of $\mathbf{9}^+$. The k_2 and k_4 values used in the CV simulations were estimated, in qualitative agreement with the DFT barriers, and were fixed in the CV simulations ($k_2 \approx 2000\ s^{-1}$, $k_4 \approx 0.02\ s^{-1}$, see Supporting Information for details). All other rate and equilibrium constants were optimized (Scheme S1, Supporting Information). Fast bimolecular coupling to $\mathbf{7}^{2+}$ ($k > 10^7\ M^{-1}s^{-1}$; see Scheme 2) is indicated by the fact that 0.5 equiv. of $\mathbf{9}^+$ are produced even at low concentrations and high scan rates.[11]

In line with the IR-SEC observations (i.e. species A in Figure 5), formation of a short-lived dinuclear intermediate $[(PNP)_2Rh_2(N)(N_3)]^{2+}$ (formed in an equilibrium reaction involving $\mathbf{8}^+$ and $\mathbf{9}^+$) was included in the CV simulations.

Interestingly, additional cyclic voltammetry experiments revealed that complex **5** acts as a catalyst in electrochemical azide oxidation in the presence of an excess of N_3^- (Figure 6, red curve). Azide oxidation in the presence of $[Rh(N_3)(PNP)]$ or $[Rh(N_2)(PNP)]PF_6$ occurs at a substantially lower potential than direct azide oxidation at the Pt electrode (+0.45 V vs. $Fc^{+/0}$). The onset of the catalytic wave coincides with the first oxidation wave of **5**. Interestingly, the catalytic peak potential (E_p) shifts to slightly higher value in the presence of higher azide concentrations (Figure 6; 4-fold excess azide (red) vs. 40-fold excess azide (blue)). This observation is rationalized with substrate inhibition by (reversible) azide coordination to one or more of the intermediates shown in Scheme 2, thus slowing down the electrocatalysis. For example, azide coordination to $\mathbf{7}^{2+}$ stabilizes the complex in the form of $\mathbf{10}^+$, which was characterized crystallographically. Electrocatalytic azide anion oxidation is potentially relevant for the design of (novel) azide-based fuel cells, expelling only harmless dinitrogen gas as the exhaust gas.[13] Azide anion oxidation has also been proposed as one of the key-steps in Pt-catalysed electro-oxidation of ammonia in direct ammonia fuel cells.[14] As such, the mechanistic insights and results described in this paper might well be relevant for research and development of non-carbon-based fuel cells.[3d]

In conclusion, one-electron oxidation of the rhodium(I) azido complex $[Rh^I(N_3)(PNP)]$ (**5**), bearing a neutral, pyridine-based PNP ligand, leads to instantaneous and selective formation of the mononuclear rhodium(I) dinitrogen complex $[Rh^I(N_2)(PNP)]^+$ ($\mathbf{9}^+$). Interestingly, in the presence of excess azide, complex **5** also acts as electrocatalyst for electrochemical azide oxidation. This is of potential relevance for the design of azide-based fuel cells, expelling only harmless dinitrogen gas as the oxidized product. The mechanism of N_3^- oxidation in these processes is non-trivial. Rather than the previously observed formation of a rhodium–nitridyl intermediate $Rh(N^\bullet)(PNP)$ undergoing N–N coupling as observed for related neutral complexes (bearing an anionic PNP pincer), the cationic $[Rh^{II}(N_3)(PNP)]^+$ intermediate $\mathbf{6}^+$ appears to react via an entirely different mechanism. DFT studies and supporting experimental observations suggest a pathway involving formation of the mixed-valent dinuclear $[(PNP)Rh^I(\mu\text{-}N_3)Rh^{III}(N_3)(PNP)]^{2+}$ species $\mathbf{7}^{2+}$, which fragments via N–N bond splitting to form 0.5 equivalents of $[Rh^I(N_2)(PNP)]^+$ ($\mathbf{9}^+$) and $[Rh^V(N)(N_3)(PNP)]^+$ intermediate $\mathbf{8}^+$. Subsequent intramolecular azide attack at the terminal nitrido moiety of the formally rhodium(V) azido–nitrido intermediate $\mathbf{8}^+$ then produces a second 0.5 equiv. of $\mathbf{9}^+$. The cationic charge of $[Rh^{II}(N_3)(PNP)]^+$ complex $\mathbf{6}^+$ might contribute to the deviating pathway when compared to the mechanism reported earlier for neutral $[M^{II}(N_3)(PNP)]$ complexes (M = Rh, Ir). Further studies to investigate the intriguing reactivity of group 9 transition-metal nitride complexes are underway in our laboratories.

Experimental Section

All reactions were carried out under an atmosphere of nitrogen or argon using standard Schlenk techniques. The following compounds were prepared following literature procedures: [(PNP*t*Bu)Rh(Cl)].[6] Other reagents were purchased from commercial suppliers and used without further purification. THF, pentane, toluene and Et_2O were distilled under an inert atmosphere from sodium/benzophenone ketyl and MeOH from CaH_2. NMR spectra (^1H, $^1H\{^{31}P\}$, ^{31}P, $^{31}P\{^1H\}$, ^{31}P-^1H, and $^{13}C\{^1H\}$) were measured on a Varian INOVA 500 MHz, a Bruker AV400 or a Varian MERCURY 300 MHz spectrometer. IR spectra were recorded with a Bruker Alpha-p FT-IR spectrometer (ATR) or with a Thermo Nicolet nexus FT-IR spectrometer (solution). High resolution mass spectra were recorded on a JEOL JMS SX/SX102A four sector mass spectrometer; for FAB-MS 3-nitrobenzyl alcohol was used as a matrix. Cold-spray ESI-MS measurements were performed on JEOL AccuTOFLC-plus JMS-T100LP spectrometer. Cyclic voltammetry measurements were performed in THF containing $[(nBu)_4N]F_6$ (0.1 M) at room temperature under a nitrogen atmosphere, using an Autolab PGSTAT302N potentiostat, a three-electrode cell containing a platinum disk working electrode ($r = 0.029$ cm), a platinum coil counter electrode and a silver wire reference electrode. All redox potentials are referenced to $Fc^{+/0}$ added as an internal standard. Spectro-electrochemical IR (SEC-IR) experiments were performed with an optically transparent thin-layer electrochemical (OTTLE) cell, developed in house (design: F. Hartl). Digital simulations of the cyclic voltammetry data were carried out using DigiElch8.FD software.[15] See Supporting Information for synthetic procedures and characterisation data of complex **5** and [**9**](PF_6).

Acknowledgements

Financial support from the Netherlands Organization for Scientific Research (NWO-CW VICI project 016.122.613) and the University of Amsterdam (Research Priority Area Sustainable Chemistry) is gratefully acknowledged. I.S. thanks the DFG (SI 1577/2-1) for financial support. J.I.v.d.V. thanks Dr. M.A. Siegler (John Hopkins University) for tips and tricks regarding X-ray crystallography.

Conflict of interest

The authors declare no conflict of interest.

Keywords: dinitrogen complexes · EPR spectroscopy · fuel cells · nitrido · rhodium

[1] J. R. Jennings, Catalytic Ammonia Synthesis: Principles and Practice; Plenum: New York, **1991**.

[2] a) L. A. P. Kane-Maguire, P. S. Sheridan, F. Basolo, R. G. Pearson, *J. Am. Chem. Soc.* **1970**, *92*, 5865; b) J. D. Buhr, H. Taube, *Inorg. Chem.* **1979**, *18*, 2208; c) C.-M. Che, H.-W. Lam, W. F. Tong, T.-F. Lai, T.-C. Lau, *J. Chem. Soc. Chem. Commun.* **1989**, 1883; d) D. C. Ware, H. Taube, *Inorg. Chem.* **1991**, *30*, 4605; e) K. D. Demadis, T. J. Meyer, P. S. White, *Inorg. Chem.* **1997**, *36*, 5678; f) O. Krahe, E. Bill, F. Neese, *Angew. Chem. Int. Ed.* **2014**, 8727; g) C. Rebreyend, B. de Bruin, *Angew. Chem. Int. Ed.* **2015**, *54*, 42 – 44; *Angew. Chem.* **2015**, *127*, 42 – 44; h) N. Khoenkhoen, B. de Bruin, J. N. H. Reek, W. I. Dzik, *Eur. J. Inorg. Chem.* **2015**, *4*, 567 – 598.

[3] a) Y. Gloaguen, C. Rebreyend, M. Lutz, P. Kumar, M. Huber, J. I. Van der Vlugt, S. Schneider, B. de Bruin, *Angew. Chem. Int. Ed.* **2014**, *53*, 6814 – 6818; *Angew. Chem.* **2014**, *126*, 6932 – 6936; b) M. G. Scheibel, B. Askevold, F. W. Heinemann, E. J. Reijerse, B. de Bruin, S. Schneider, *Nat. Chem.* **2012**, *4*, 552 – 558; c) M. G. Scheibel, Y. Wu, A. C. Stückl, L. Krause, E. Carl, D. Stalke, B. de Bruin, S. Schneider, *J. Am. Chem. Soc.* **2013**, *135*, 17719 – 17722; d) M. G. Scheibel, J. Abbenseth, M. Kinauer, F. W. Heinemann, C. Würtele, B. de Bruin, S. Schneider, *Inorg. Chem.* **2015**, *54*, 9290 – 9302; e) J. Abbenseth, M. Finger, C. Würtele, M. Kasanmascheff, S. Schneider, *Inorg. Chem. Front.* **2016**, *3*, 469 – 477.

[4] a) C. C. Hojilla Atienza, A. C. Bowman, E. Lobkovsky, P. J. Chirik, *J. Am. Chem. Soc.* **2010**, *132*, 16343 – 16345; b) J. Schöffel, N. Susnjar, S. Nückel, D. Sieh, P. Burger, *Eur. J. Inorg. Chem.* **2010**, 4911 – 4915.

[5] a) E. M. Zolnhofer, M. Käß, M. M. Khusniyarov, F. W. Heinemann, L. Maron, M. van Gastel, E. Bill, K. Meyer, *J. Am. Chem. Soc.* **2014**, *136*, 15072 – 15078; b) V. Vreeken, B. de Bruin, M. A. Siegler, J. I. van der Vlugt, *Dalton Trans.* **2017**, *46*, 7145 – 7149.

[6] D. Hermann, M. Gandelman, H. Rozenberg, L. J. W. Shimon, D. Milstein, *Organometallics* **2002**, *21*, 812.

[7] The analogous triflate salt of N_2-complex $\mathbf{9}^+$ has been reported previously: S. K. Hanson, D. M. Heinekey, K. I. Goldberg, *Organometallics* **2008**, *27*, 1454.

[8] Formation of rhodium(II) species $\mathbf{9}^{2+}$ in this experiment is due to over-oxidation of rhodium(I) complex $\mathbf{9}^+$, caused by a local higher Fc^+ concentration upon mixing-in a solution of [Fc](PF_6) into a solution of **5**, followed by rapid freeze-quenching.

[9] a) K. D. Demadis, E.-S. El-Samanody, T. J. Meyer, P. S. White, *Inorg. Chem.* **1998**, *37*, 838 – 839; b) K. D. Demadis, T. J. Meyer, P. S. White, *Inorg. Chem.* **1998**, *37*, 3610 – 3619.

[10] Related [(NNN)Ir(μ-N_3)Ir(NNN)] complexes have been reported, which form nitrido-bridged [(NNN)Ir(μ-N)Ir(NNN)] species upon photolysis or thermolysis (100 °C, 1 day): F. Angersbach-Bludau, C. Schulz, J. Schoffel, P. Burger, *Chem. Commun.* **2014**, *50*, 8735 – 8738.

[11] Notably, the fast (diffusion limited) bimolecular coupling step k_1 compares with much slower rate constants derived for bimolecular nitride coupling reactions shown in Scheme 1. See references [3b–e].

[12] R. Battino, Ed., IUPAC Solubility Data Series, Volume 10: Nitrogen and Air, Pergamon Press, Oxford, 1982; online available at https://srdata.nist.gov/solubility/IUPAC/SDS-10/SDS-10.pdf (retrieved August 25, 2017).

[13] R. C. Bohannon, U.S. Patent No 4421829, US4421829 (A), December 20, **1983**.

[14] a) F. J. Vidal-Iglesias, J. Sola-Gullón, J. M. Peréz, A. Aldaz, *Electrochem. Commun.* **2006**, *8*, 102 – 106; b) F. J. Vidal-Iglesias, J. Solla-Gullón, J. M. Feliu, H. Baltruschat, A. Aldaz, *J. Electroanal. Chem.* **2006**, *588*, 331 – 338.

[15] DigiElch Professional Version 8.FD; ElchSoft GbR: Kleinromstedt, Germany, **2006**.

Manuscript received: June 26, 2017
Accepted manuscript online: September 12, 2017
Version of record online: October 12, 2017

